Modeling and Control of Dielectric Elastomer Enabled Cuff Device for Enhancing Blood Flow at Lower Limbs

Theophilus Kaaya, Rahul J. Venkatraman, Denizcan Koc, Zheng Chen*

Abstract—Orthostatic hypotension, deep vein thrombosis (DVT), and edema are venous system disorders that affect the lower limbs and are common causes of decreased work performance and affect the lives of many individuals. Compression devices, rotation of staff, and regular breaks can alleviate these problems. Active compression devices use air compression and require a pump, making them bulky. A calf muscle device that uses a dielectric elastomer as a soft actuator that is compact, lightweight, and resilient, making it convenient for use is developed. In this study, a physics-based model of the device is presented by combining the physics of a thin-walled dielectric elastomer vessel with the force interactions between the active vessel and the cylindrical passive elastomer within. The couplings between the two nonlinear elastic models are solved and a controloriented model that is capable of capturing the pressure change experienced by the device under an applied voltage is established. A prototype of the device is made and characterized. The model is validated in the normal frequency range of the device. Human pulse signal tracking is then performed using adaptive iterative learning control (ILC) in a feedback loop. Experimental results have shown that the device can generate up to 10 Pa fluid pressure difference while tracking a human pulse signal with almost zero phase delay.

Keywords- Dielectric elastomer actuators, wearable devices, modeling, iterative learning control

Note to Practitioners: This paper describes a method that enhances blood flow using a comfortable soft cuff device. The device is made of dielectric elastomer which can generate contractions when it wraps around a lower limb to help circulate blood flow. Development of the cuff device could provide a preventive and proactive tool, as well as a rehabilitation tool, for regulating and improving blood flow. For example, this device could help a passenger who takes a long time flight to circulate his/her blood flow. This device could also help an athlete improve his/her muscle performance in highly intensive competitions. This paper details design, modeling, fabrication, and control of the device. A prototype of the device was fabricated and was able to generate enough contractions on an artificial lower limb to influence the blood pressure while tracking a human pulse signal. Experimental results have shown a great promise in enhancing blood flow with such a wearable and comfortable device.

I. INTRODUCTION

The body's circulatory system delivers oxygen and other nutrients to muscles, connective tissues, organs, and other cellular components [1], [2]. To function effectively, the muscular system relies on oxygen and nutrients carried by the blood. Muscles, particularly those in the lower limbs, can require little amounts of oxygen to high amounts of oxygen depending on the amount of physical activity performed at any given time. Cardiovascular strength is constantly needed during physical exercise to overcome gravity pulls and to adjust to different body positions, such as standing. During postural shifts, gravitational effects are critical, particularly in controlling any venous blood pooling [3], [4].

Inadequate blood supply prevents involuntary or voluntary contracted muscles from relaxing, resulting in claudication [5], (muscle discomfort), cramps, spasms, strains, and tears. Astronauts face identical problems in space as well as when they return to Earth. Reduced gravity forces limit stroke volume (SV), which is the amount of blood expelled from the heart [6], resulting in a loss of muscle mass. This can result in orthostatic intolerance (OI), which is the inability to adjust and maintain blood pressure while standing. Even with post-flight rehabilitation, the human body might go through a painful process, especially in the lower limbs [7], [8].

Development of a cuff device could provide a preventative and proactive tool, as well as a rehabilitation tool, for regulating and improving blood flow. The mechanics, materials, and control system employed to produce a robust design are what make such gadgets unique. Air compression devices [9] that need the use of motors and pumps to generate the compression force or negative pressure chambers for muscle recovery [10], [11] are examples of traditional devices that have been used. These methods necessitate the employment of cumbersome instruments that take up a significant amount of space [12].

Our previous research has shown that compression devices using a dielectric elastomer actuator (DEA) provide a lowcost, lightweight, comfortable, daily use, and portable method for generating pressure change to regulate and increase blood flow in the lower limbs [13]. DEAs are light, flexible materials that deform in response to electrical stimulation. DEAs are attractive to biomorphic robots because of their electromechanical properties [14]–[16]. Some of the drawbacks of DEAs as compression devices are the need to use a high voltage and the magnitude of the output pressure is limited by the material composition and pre-stretch. It is necessary to determine the optimal pre-stretch that produces the maximum compression pressure change for a given material. The high voltage requirement is traded with the low power consumption of the actuator. A compression sleeve is also added as a layer betweeen the calf and the DEA for added protection.

The basic operation of DEAs works on the principal that applying voltage across the membrane induces deformation while withdrawing voltage restores the membrane to its normal

^{*}Corresponding author: Zheng Chen, Email: zchen43@central.uh.edu. This work is supported in part by the National Science Foundation under Grant CMMI #1747855.

T. Kaaya, R. Venkatraman, D. Koc, and Z. Chen are with the University of Houston, Mech. Eng. Dept, 4800 Calhoun Rd, Houston TX 77004. tskaaya@uh.edu, rjvenkatraman@uh.edu, dkoc3@uh.edu, zchen43@central.uh.edu

shape [17]. The use of DEAs in this way necessitates the generation of a periodic pressure change which is needed in a compression device for enhancing blood flow. Multiple layers of dielectric (DE) material can be stacked or rolled to achieve high pressure change. Using rolled or stacked actuators to generate a macro-sized pressure change can take hundreds of layers, as shown in [18] where $0.16 \ N/mm^2$ of actuation pressure for a stack-actuator is achieved. An active compression bandage (ACB) made with DEAs showed a pressure change of 5.2 percent for a single layer activated at 11.3 kV, while a pressure change of 8.0 percent for three layers was simulated using the Ogden density function in an analytical physics model [19]. Through continuous actuation, this work revealed the impact of electrical input and elastomer geometry on pressure change. When continuously actuated at 1.2 kV, a DEA-spring design that is also used for active compression recorded a pressure change of roughly 2.5 mmHg (333.31 Pa) with a starting pressure of 26 mmHg (3466.38 Pa) [20]. It's worth mentioning that a healthy person's net blood pressure, or the difference between their systolic and diastolic blood pressures (120/80), is 40 mmHg (5333 Pa), making the location of the unactuated (highest) and actuated (lowest) pressures crucial to performance. The maximum pressure is used as the base pressure for the device to operate in order to cause large pressure changes and improve blood flow.

Different compression device configurations have been presented. A strip DE actuator is attached to a retaining spring and belt mechanism in [20], to achieve device compression and relaxation. For both compression and relaxation of the device, Shahram Pourazadi et al use a single layer DE bandage [19]. Shahram Pourazadi et al used an input-output linearizer controller to accomplish nonlinear control of pressure reference tracking in order to operate these compression devices [21]. Zhihang Ye et al used an H_{∞} controller to handle model uncertainty, disturbance rejection, and sensor noise to show robust control of a diaphragm actuator for human pulse signal tracking. One of the challenges faced with controllers that rely on feedback loop signal control is phase delay. Iterative learning control (ILC) has been presented as a solution to eliminate phase delay in periodic tracking problems. The control has found use in a variety of disciplines, including mechanical testing, factory robots, and health-care rehabilitation robotics

A quasi static physical model to show total pressure of a DEA compression device has been derived in work done by Pourazadi *et al* [19], and the basis for developing a dynamic-based model is shown in work by Kaaya *et al* [27] using the frequency response analysis. L Calabrese *et al* demonstrated an active bandage design with one roll turn [28] however, no control or coupling between the DEA and the calf was presented in their work. A prototype of the DEA device was fabricated and characterized in our prior work [13]. The presentation of a physics-based dynamical model for the calf muscle device, which captures the nonlinear elasticity of a thin walled dielectric elastomer vessel with the force interactions between the thin vessel and the passive cylindrical elastomer around which the device is attached, is one of the major contributions in this paper. The model also incorporates an

electrical impedance model of the dielectric with aforementioned nonlinear elasticity and comes up with a nonlinear state space representation for controller and estimator design purposes. Since the capacitance changes with the thickness of the DE cuff, the impact of the nonlinear elasticity on the steady-state error is investigated and the analysis shows that ILC can reduce the steady-state error to zero when a step reference is applied.

The pressure inside the blood vessel is normally not measurable in real-time, the nonlinear elastic part of the model is also used to predict this pressure which is used to quantify the performance of the DEA in helping the calf muscle to generate enough pressure to open and close the blood vessel valve in order to prevent blood pooling. In addition to this, since the model is physics-based, the model can be used to select material property, pre-stretching rate, and number of layers of the DE cuff and to design one to achieve a given control goal with suitable bandwidth, by adjusting and optimizing various parameters. Finally, an adaptive ILC is designed and implemented in real-time to track a reference signal planned from a human pulse signal. ILC can adjust to model aspects that the mathematical model ignores. These unmodeled aspects are contained in the error signal from which the ILC learns from. The device with ILC can generate meaningful pressure change which causes fluid contact angle change as observed in an artificial vein simulate.

The remainder of the paper is organized as follows: Section II describes the methodology that discusses the design and fabrication of the dielectric elastomer calf muscle device (DECMD) in II-A. The modeling of the DECMD is then covered in Section II-B. The design and analysis of the adaptive ILC is covered in Section II-C. Then, the experimental setup and model validation are addressed in Section III, and the conclusion and future work are described in Section IV.

II. METHODOLOGY

A. Design and Fabrication

The operating principal of a DEA as mentioned in section I is primarily through the actuation of a dielectric membrane using Maxwell pressure when an electric field is applied across the membrane. The electric field is achieved through the application of a voltage potential across compliant electrodes that are placed on the dielectric membrane having the membrane sandwiched by the electrodes. This configuration makes the DEA behave as a capacitor. To account for strain hardening of the DEA and the calf muscle during actuation, the couplings between the two are calculated using the Gent model. The pressure change experienced by the device under the input voltage applied to the DE, as well as the pressure induced inside the passive layer, are then captured using the control-oriented model. This pressure is interpreted as blood pressure within the vein.

1) DECMD Cuff Design: As shown in Figure 1, a DEA strip is rolled twice over a compression sleeve for this design. The stretches defined in the figure are the longitudinal direction, radial direction, and circumferential direction which are represented as λ_1, λ_2 and λ_3 respectively. The number

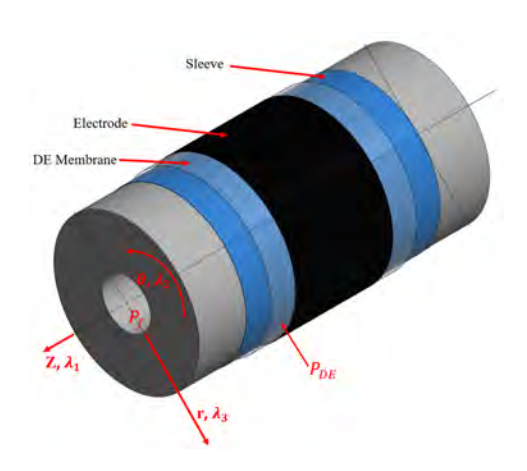


Fig. 1. DECMD Design

of roll turns increases as the number of layers increases. This, in turn, increases the force output [29]. The force decreases as the elastomer expands radially rather than increasing with applied voltage. The multi-layer DEA strip, in conjunction with the compression sleeve, increases venous pressure. Actuating voltage from 0 V to the desired input causes a periodic change in applied pressure (compression) and released pressure (relaxation). Blood flow is reduced when pressure is applied, but it increases when pressure is released.

The innermost layer of the DEA Cuff is a thin compression sleeve. This layer serves as a thermal and insulating barrier, preventing any electrical contact between the DECMD electrodes and the skin of the lower limb. The thin material also allows the actuator to provide minimal resistance to motion. Following the compression layer is a two-layer rolled actuator made up of elastomer and painted electrodes. Section II-A2 goes over the procedure for applying the DEA layer and compression sleeve.

Figure 2 shows a cross section of the DEA in the unactuated(compression) and actuated(relaxation) state. In order to

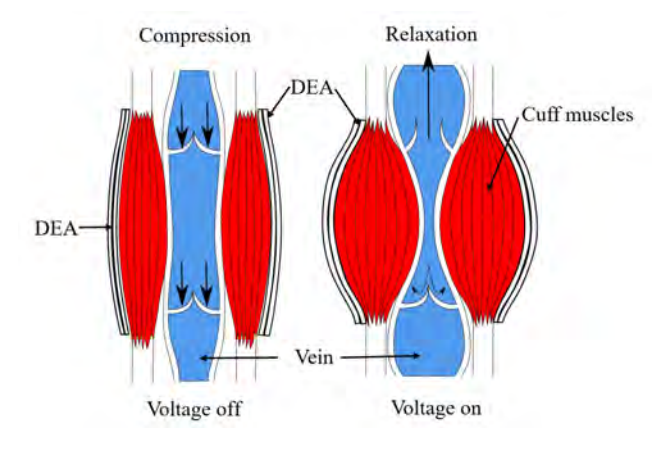


Fig. 2. Sketch of the DECMD during compression and relation

enhance blood flow, the DECMD is employed to compress the calf muscle in turn constricting the vessels. The veins are more compliant than the arteries and as such will constrict more than the arteries [30]. This helps ensure there is no venous back flow by completely closing the valves as well as increasing or

maintaining the blood pressure during posture changes. As a result, orthostatic intolerance can be mitigated.

2) DEA Cuff Fabrication: The DEA strip is made from 3M 4910 very high bond (VHB) tape serving as the dielectric elastic membrane. For this experiment, a 30 cm x 6.5 cm x 1 mm DEA strip is cut as shown in Figure 3. For electrode

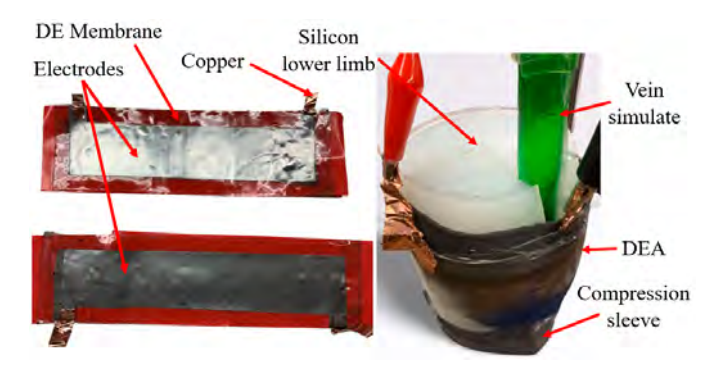


Fig. 3. DEA strips and cuff application

application a 1.5 cm margin is made from each side of the elastomer to avoid short circuits at the edges. The red VHB protective layer is applied to the border to facilitate electrode application. The rest of the membrane is painted with graphite powder, which was chosen as the electrode. The border is then removed and used to measure small painting regions that extend from the electrode area in order to attach copper tape. The copper tape strip is cut and applied to the small painted area. To avoid a short circuit or electric contact with any other adjacent components, careful painting is required. The painted membrane is flipped over, and the painting and lead attachment procedures are repeated as in the first case. The positive and negative connections to the power supply are provided by the two opposing leads.

The DEA Cuff is attached to the calf section by rolling the DEA strips to the desired number of turns. Then the rolled strip is stretched circumferentially to a diameter larger than the silicon calf simulate. The calf simulate is then inserted inside the rolled DEA and finally the strip is released to grip the calf simulate. The calf section is scaled down by a ratio of 1:2.25. The scale-down factor is based on the limited 3D printing space for the calf mold. Ecoflex 00-30 two-part mixture silicone rubber is used to approximate the elastic stiffness of the calf muscle. The reported 100% Modulus of the silicon is about 69 KPa. This value is within the reported range of calf muscles [31], [32]. In a 3D printed mold, a large amount of silicone mixture is poured and cured. Following curing, the silicone muscle is removed and aired out again to ensure solidity. To simulate the vein, a fluid bag containing colored water is used. The excess fluid is poured into a cup after a tiny hole is pierced. This tiny piercing is designed in such a way that a flexible rubber tube can be inserted and glued to a plastic tube. This tube represents a superficial capillary that is used to detect changes in fluid pressure. The liquid is then re-poured into the plastic casing via the rubber tube with a fluid syringe and sealed to increase fluid pressure. To insert the fluid bag, a thin wedge is sliced into the back of the calf section. The location of the fluid bag is close to that of the saphenous vein adjacent to the calf muscle. As a result, the muscle puts pressure on the vein. As shown in Figure 3, the compression sleeve (Tommie Copper®) is then wrapped around the silicone muscle, and the DEA strip is wrapped around the sleeve 2 times to achieve a prestretch of 200%. For this DEA cuff, a maximum pressure of 52 mmHg was achieved.

B. Modeling of the DECMD

As previously described, the dielectric elastomer (DE) strip is rolled n times over a compression sleeve, as shown in Figure 4. To achieve the desired prestretch in the DEA, the

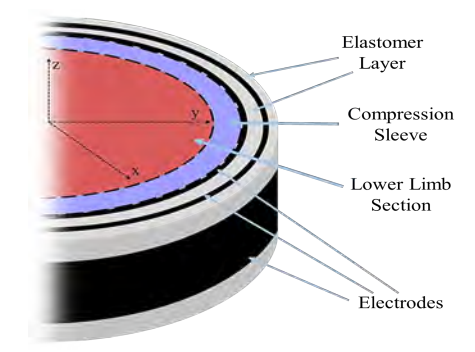


Fig. 4. Cross-sectional design of the DECMD

DEA strip is rolled over the calf. Because of the elastic energy stored in the membrane, this causes a contact pressure to be exerted on the calf. When a voltage is applied, the contact pressure decreases as the elastomer expands radially. The multi-layer DEA strip, in conjunction with the compression sleeve, increases venous pressure.

The DECMD is modeled as a tubular actuator with multiple layers stacked on top of one another. The elastic energy stored in the dielectric membrane causes the DECMD to exert pressure P_{DE} around the calf at the inner surface of the membrane. Let the inner surface be A. The outer surface of the membrane, B is exposed to the atmosphere. Activating the DECMD electrically relaxes the dielectric membrane, relieving pressure P_{Φ} on the calf. This pressure interaction, in turn, exerts pressure change on the blood vessels within the calf, resulting in an increase in blood flow.

The Gent model is used to simulate the actuator's elasticity, with the Helmholtz's energy, W given as

$$W = -\frac{\mu J}{2} \ln \left(1 - \frac{I_1 - 3}{J} \right) \tag{1}$$

where μ is the actuator's shear modulus, J is the limiting stretch, $I_1 = \lambda_1^2 + \lambda_2^2 + \lambda_3^2$ is the first principle invariant, and λ_i the stretch in the longitudinal, circumferential, and radial direction, for i=1,2,3 respectively. Taking the reference coordinate system as (R,Θ,Z) and the current coordinate system as (r,θ,z) , and assuming symmetric deformation in the circumferential direction, let $\lambda_1 = \lambda_z = z/Z$, $\lambda_2 = \lambda = r/R$, and $\lambda_3 = (\lambda \lambda_z)^{-1} = h/H = dr/dR$. h is the current membrane thickness and H is the undeformed membrane thickness. The

dielectric membrane is assumed to be an isotropic incompressible material [33].

The deformation gradient, F is therefore given by

$$\mathbf{F} = \begin{bmatrix} \lambda_1 & 0 & 0 \\ 0 & \lambda_2 & 0 \\ 0 & 0 & \lambda_3 \end{bmatrix} \tag{2}$$

The Left Cauchy-Green deformation tensor, B is

$$\mathbf{B} = \mathbf{F}\mathbf{F}^T \begin{bmatrix} \lambda_1^2 & 0 & 0 \\ 0 & \lambda_2^2 & 0 \\ 0 & 0 & \lambda_3^2 \end{bmatrix}$$
 (3)

The Cauchy stress tensor is given by

$$\sigma = -p\mathbf{I} + \frac{\mu J}{J - (I_1 - 3)}\mathbf{B} \tag{4}$$

where p is the hydro-static pressure. Substituting for **B** in equation 4 gives

$$\sigma_{rr} = -p + \frac{\mu J(\lambda \lambda_z)^{-2}}{J - (I_1 - 3)} \tag{5}$$

$$\sigma_{\theta\theta} = -p + \frac{\mu J \lambda^{-2}}{J - (I_1 - 3)} \tag{6}$$

$$\sigma_{zz} = -p + \frac{\mu J \lambda_z^{-2}}{J - (I_1 - 3)} \tag{7}$$

In the absence of body forces, the equilibrium equation in the radial direction becomes [33]

$$\frac{d\sigma_{rr}}{dr} + \frac{1}{r}(\sigma_{rr} - \sigma_{\theta\theta}) = 0 \tag{8}$$

with the following boundary conditions; the stress on the outer surface of the membrane $\sigma_{rr}(b) = 0$ while that at the inner surface $\sigma_{rr}(a) = -P_{el}$. P_{el} is the elastic pressure exerted by the actuator on the calf muscle. Taking the integral of Eq. 8 and applying the boundary conditions gives

$$\int_{-P_{el}}^{0} d\sigma_{rr} = \int_{a}^{b} \frac{1}{r} (\sigma_{\theta\theta} - \sigma_{rr}) dr \tag{9}$$

Substituting for $\sigma_{\theta\theta}$ and σ_{rr} gives

$$P_{el} = \int_{a}^{b} \frac{1}{r} \left[\frac{\mu J \lambda^{-2}}{J - (I_1 - 3)} - \frac{\mu J (\lambda \lambda_z)^{-2}}{J - (I_1 - 3)} \right] dr$$
 (10)

Using $dr/dR = (\lambda \lambda_z)^{-1}$ and taking the implicit derivative of $\lambda = r/R$, one can arrive at the expression $dr = \frac{R}{1-\lambda^2 \lambda_z} d\lambda$. Substituting this in Eq.10 gives

$$P_{el} = \int_{\lambda_a}^{\lambda_b} \frac{1}{\lambda} \frac{\mu J}{J - (I_1 - 3)} \frac{\left(\lambda^{-2} - (\lambda \lambda_z)^{-2}\right)}{1 - \lambda^2 \lambda_z} d\lambda \tag{11}$$

such that $\lambda_a = a/A$ and $\lambda_b = b/B$.

The assumption of incompressibility implies that there will be no volume change. This means that $(r^2 - a^2)\pi z = (R^2 - A^2)\pi Z$. Diving through by πZ and substituting for $r = \lambda R$ gives

$$R^2(\lambda^2\lambda_z - 1) = a^2\lambda_z - A^2 \tag{12}$$

Substituting for $\lambda = \lambda_b$ and $a = \lambda_a A$ when R = B yields

$$\lambda_a^2 \lambda_z - 1 = \left(\frac{B}{A}\right)^2 (\lambda_b^2 \lambda_z - 1) \tag{13}$$

$$\lambda_a^2 \lambda_z - 1 = (\varepsilon + 1)^2 (\lambda_b^2 \lambda_z - 1) \tag{14}$$

For a thin walled cylinder, $\varepsilon \ll 1$. Therefore $(\varepsilon + 1)^2 \approx 2\varepsilon + 1$. Eq.14 simplifies to

$$(\lambda_a - \lambda_b)(\lambda_a + \lambda_b)\lambda_z = 2\varepsilon(\lambda_b^2 \lambda_z - 1) \tag{15}$$

Also for the thin walled cylinder, $\lambda_a \approx \lambda_b \approx \lambda$. From Eq. 15 this yields

$$\lambda_a - \lambda_b = \frac{\varepsilon}{\lambda \lambda_z} (\lambda_b^2 \lambda_z - 1) \tag{16}$$

and Eq.11 becomes

$$P_{el} = \frac{1}{\lambda} \frac{\mu J}{J - (I_1 - 3)} \frac{\left(\lambda^{-2} - (\lambda \lambda_z)^{-2}\right)}{1 - \lambda^2 \lambda_z} \int_{\lambda_a}^{\lambda_b} d\lambda$$
 (17)

Therefore

$$P_{el} = \frac{\mu_d \varepsilon_d J_d n \left[\lambda_d^2 - (\lambda_d \lambda_{zd})^{-2} \right]}{\left[J_d - (I_{1d} - 3) \right] \lambda_d^2 \lambda_{zd}}$$
(18)

where $\varepsilon_d = \frac{H}{R_d}$ denotes the DECMD's geometric curvature. R_d is the mean radius of the DECMD in the undeformed state. The DECMD's properties are represented by the subscript d.

The pressure due to Maxwell stress, P_{Φ} , assuming a small walled vessel is given as [34]

$$P_{\Phi} = \sigma_{\Phi} - \frac{h}{r} \tag{19}$$

where $\sigma_{\Phi} = \varepsilon E^2/2$ is the Maxwell stress. Approximation using a parallel plate capacitor gives $E = \Phi/h$. Therefore

$$P_{\Phi} = \frac{\varepsilon_e n \lambda_{zd}}{2HR_d} \Phi^2 \tag{20}$$

where ε_e is the dielectric membrane permittivity and Φ is the voltage applied on the DECMD membrane. Since the elastic pressure exerts pressure to the calf and the maxwell pressure relieves it, the pressure P_{DE} at the DECMD calf interface is

$$P_{DE} = P_{el} - P_{\Phi} \tag{21}$$

$$P_{DE} = \frac{\mu_d \varepsilon_d J_d n \left[\lambda_d^2 - (\lambda_d \lambda_{zd})^{-2} \right]}{\left[J_d - (I_{1d} - 3) \right] \lambda_d^2 \lambda_{zd}} - \frac{\varepsilon_e n \lambda_{zd}}{2H R_d} \Phi^2$$
 (22)

Assume the calf muscle and blood vessel to be tubular and concentric. The pressure at the interface between the DECMD and the calf muscle is the same, P_{DE} while the pressure inside the vessel is P_f . Eq. 8 for the calf-vessel becomes

$$\int_{-P_f}^{-P_{DE}} d\sigma_{rr} = \int_a^b \frac{1}{r} (\sigma_{\theta\theta} - \sigma_{rr}) dr$$
 (23)

Integrating as from Eq.10-18 gives

$$-P_{DE} + P_f = \frac{\mu_m \varepsilon_m J_m \left[\lambda_m^2 - (\lambda_m \lambda_{zm})^{-2} \right]}{\left[J_m - (I_{1m} - 3) \right] \lambda_m^2 \lambda_{zm}}$$
(24)

where the subscript m represents the properties of the calf muscle. At the interface, $r = \lambda_d R_d^B$ and $r = \lambda_m R_m^B$. Therefore

Let $\frac{B}{A} = \frac{B-A}{A} + 1 = \varepsilon + 1$. ε is the geometric curvature. This $\lambda_m = \frac{\lambda_d R_d^B}{R_m^B}$. Assuming $\varepsilon_m = \alpha \varepsilon_d$, $\mu_m = \beta \mu_d$, $J_m = J_d$, $\lambda_{zm} = implies$ that $\lambda_{zd} = \lambda_{z}$, and $I_{1m} \approx I_{1d}$ for simplicity, P_f is given by

$$P_{f} = \frac{\mu \varepsilon J \left[\lambda^{2} \left(n + \alpha \beta \right) - (\lambda \lambda_{z})^{-2} \left(n + \alpha \beta \left(\frac{R_{d}}{R_{m}} \right)^{-4} \right) \right]}{\left[J - (I_{1} - 3) \right] \lambda^{2} \lambda_{z}} - \frac{\varepsilon_{e} n \lambda_{z}}{2HR_{d}} \Phi^{2} \quad (25)$$

 R_m is the mean radius of the calf muscle, α and β are scaling factors for the geometric curvatures and shear modulus of the DECMD and the calf muscle respectively. These factors change based on the material properties the DECMD is attached to. The subscript d is dropped for neatness.

The actuator is driven by voltage and is modeled as a classical RC series circuit such that

$$\dot{\Phi} = -\frac{\Phi}{RC} + \frac{u}{RC} \tag{26}$$

where R is the resistance of the circuit and C is the capacitance of the DE, treated as a cylindrical capacitor, given by

$$C = \frac{2\pi\varepsilon nL\lambda_z}{\ln\left(1 + \frac{H}{r\lambda_z\lambda}\right)} \tag{27}$$

The capacitance can also be employed as a feature for pressure self-sensing as well as user heart rate and blood pressure monitoring [35]–[37]. The capacitance is treated as a constant since it does not change significantly at low actuation frequencies. Self-sensing is realized when a high frequency signal is added to the actuation signal to peak out the capacitance change. Finally, the state space equation of the model is taken as

$$\dot{\Phi} = -\frac{\Phi}{RC} + \frac{u}{RC} \tag{28}$$

$$y_1 = P_{DE} \tag{29}$$

$$y_2 = P_f \tag{30}$$

where the state is the membrane voltage, Φ , the control is the input voltage, u, and the output, $y = (y_1, y_2)$ is the DECMD interface pressure, P_{DE} and the fluid pressure, P_f .

The circumferential stretch, λ , must be known to solve the problem. Given the base/operating pressure, P_{el} , and the fact that the majority pressure is due to the elastic contribution of the DECMD, λ may be calculated. Because the model developed thus far is quasi-static in the pressure output, it does not account for all viscous effects which are approximated as being linear in the plant model. As described in section III-B, a frequency response analysis is performed and model parameter estimate made to account for the actuator's frequency dependency as well as the time constant of the device.

C. Adaptive Iterative Learning Control Design

In this section, an adaptive iterative learning controller is designed for the DECMD to achieve human pulse signal tracking coordination. The goal is to minimize phase delay at any given frequency, and also perform flushing mechanism based on a set number of pulses. This allows for synchronization of the contraction and relaxation of the device with the pulse signal. The proposed controller for this action is of the following design

$$u_{k+1}(t) = u_{k+1}^f(t) + u_{k+1}^a(t) + u_k^l(t)$$
(31)

where k denotes the iteration such that u_{k+1} is the control input at the current iteration, u_k is the control input at the previous iteration. This formulation is similar to [38]. However, in this setup, $u_{k+1}^f(t)$ is a feedback PIDA controller input designed to account for shifting initial positions of the device.

$$u_k^f(t) = L(s) \left(ae_k + b \int e \, dt + c\dot{e} + d\ddot{e} \right) \tag{32}$$

L(s) is the overall gain of the controller, a,b,c, and d are the proportional, integral, derivative, and acceleration gains respectively. $e_k = \hat{y}_k - y_k$ is the error between the observed output y_k and the desired output \hat{y}_k . $u_{k+1}^a(t)$ is an adaptive control based on the model estimate of the transfer function. This input is added to account for the changing time constant of the actuator with high voltage application.

$$u_{\nu}^{a}(t) = B^{*}\hat{\theta} \tag{33}$$

where B^* is the regression matrix and $\hat{\theta}$ are the regressors. The regressors are taken from the characteristic equation of the transfer function 53 using the backwards Euler discretization method. u_k^l is the iterative learning control which takes the previous feedback control signal and learns from it to improve the overall control signal output.

$$u_{k+1}^{l}(t) = Q(s)\left(u_k^{l} + \gamma u_k^{f}\right) \tag{34}$$

 u_{k+1}^{l} is designed as a function of the error at a future time step of the previous iteration. The controller can be viewed as an optimization problem whose goal is to drive the error to zero, at which point the control remains unchanged. The optimization weights of the controller are Q(s), γ , and L(s). Q(s) may be seen as the overall control gain or as a filter for robustness of the control, whereas $\gamma Q(s)$ is the gain on the error signal in the previous iteration. γ represents the learning rate of the controller.

An ILC is chosen for signal tracking because of the repetitive nature of the human pulse. The ILC is better suited for this purpose [39]. The control can also account for overlooked system dynamics which are captured in the error signal. The block diagram of the control is shown in Figure 5. The information stored in memory is the observed output y_k and the applied control u_k at iteration k as well as the generated control u_{k+1} for the next iteration.

The controller is also analyzed for stability and steady state error evaluation. The objective of the controller is to drive the error signal to zero as $k \to \infty$. The error dynamics are analyzed by taking the Laplace transform of the linearized system. The linearized output y_1 using Taylor expansion is given by taking

$$y_1 = P_{DE} = P_{el} - B\Phi^2 (35)$$

Here $B = \frac{\varepsilon_e n \lambda_{zd}}{2HR_d}$ is the constant coefficient from the Maxwell pressure. The Taylor expansion is

$$y_{1L} = P_{el} - \left[B\Phi_{op}^2 + 2B\Phi_{op}(\Phi - \Phi_{op}) + HOT \right]$$
 (36)

$$=P_{el}+B\Phi_{op}^2-2B\Phi_{op}\Phi\tag{37}$$

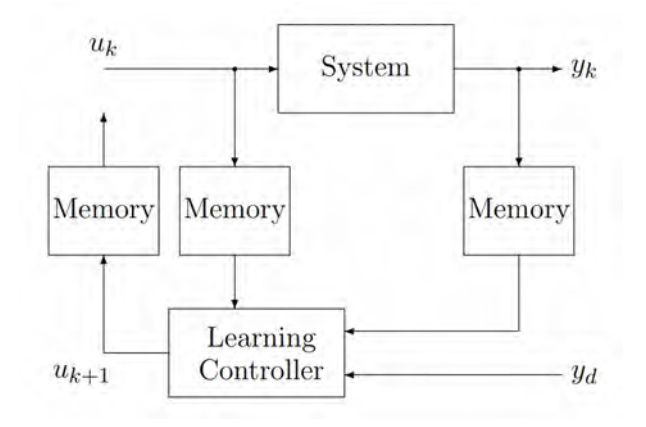


Fig. 5. Block diagram of ILC

where Φ_{op} is the voltage operating point taken at steady state and HOT are the higher order terms.

The Laplace transforms of the plant and output y_{1L} are

$$\Phi(s) = \frac{1}{RCs + 1}U(s) \tag{38}$$

$$Y_1(s) = P_{DE}(s) = \frac{P_{el}}{s} + \frac{B\Phi_{op}^2}{s} - 2B\Phi_{op}\Phi(s)$$
 (39)

and the Laplace transform of the controller is

$$U_{k+1}(s) = U_{k+1}^f(s) + U_{k+1}^a(s) + U_k^l(s)$$
(41)

where

$$U_k^f(s) = L(s) \left[a + \frac{b}{s} + cs + ds^2 \right] (Y_d(s) - Y_k(s))$$
 (42)

$$U_k^a(s) = B^*(s)\hat{\theta} \tag{43}$$

$$U_{k+1}^{l}(s) = Q(s) \left(U_{k}^{l}(s) + \gamma U_{k}^{f}(s) \right)$$
(44)

At steady state, $U_{k+1}(s) = U_k(s) = U^*(s)$. Simplifying for $U^*(s)$ in Eq. 41 gives

$$U^{*}(s) =$$

$$\frac{L(s)\left[a+\frac{b}{s}+cs+ds^{2}\right]\left[1+\gamma Q(s)\right]\left(Y_{d}(s)-\frac{P_{el}}{s}-\frac{B\Phi_{op}^{2}}{s}\right)+B^{*}(s)\hat{\theta}}{1-Q(s)-L(s)\left[a+\frac{b}{s}+cs+ds^{2}\right]\left[1+\gamma Q(s)\right]\cdot\frac{2B\Phi_{op}}{RCs+1}}$$
(45)

Using the final value theorem, the steady state error, e_{ss} subject to a step input is given as

$$e_{ss} = \lim_{s \to 0} sE(s)$$

$$e_{ss} = \left[1 - (P_{el} + B\Phi_{op}^{2})\right]$$

$$\left(1 + \frac{2B\Phi_{op}L(s)\left[a + \frac{b}{s} + cs + ds^{2}\right]\left[1 + \gamma Q(s)\right]}{1 - Q(s) - L(s)\left[a + \frac{b}{s} + cs + ds^{2}\right]\left[1 + \gamma Q(s)\right] \cdot \frac{2B\Phi_{op}}{RCs + 1}}\right)\Big|_{s=0}$$
(46)

To ensure that the steady state error goes to zero, Q(s) = 1. This implies that γ determines the rate of convergence of the

error. The limit on γ is thus dictated by the control saturation limits. L(s) is chosen as a low pass filter,

$$L(s) = \frac{1}{\tau_{s}s + 1} \tag{47}$$

where τ_s is the time constant of the filter.

III. EXPERIMENTAL RESULTS

This section describes the experimental design and setup, model identification and validation, and experimental results with ILC and PI control. The DE cuff is worn over a modeled calf muscle where the posterior tibial and saphenous veins are located for this experiment. The position of the veins is optimal for generating observable pressure changes in the veins. To validate pressure change capability and measurability, two types of experiment settings were created. To create material deformation in the DECMD, both experiments used a 20 kV high voltage amplifier (HVA) for actuation (20HVA24-P2, UltraVolt Inc).

A. Experiment Setup and Measurement

Figure 6 shows the experimental setup of the DECMD. A

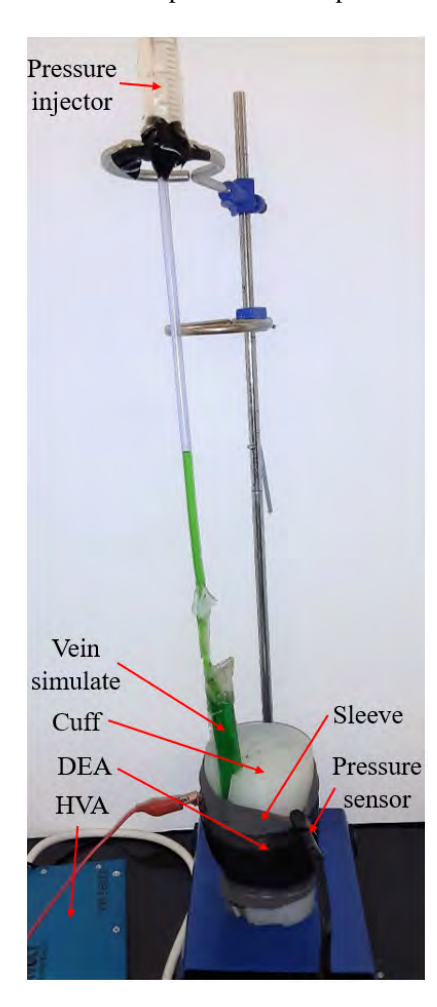


Fig. 6. Experiment setup for measuring fluid pressure with sensor

syringe is placed at the end of the rubber tube, allowing more liquid to be added to increase or decrease fluid pressure by

changing the syringe injector. To measure the change in force exerted on the vein at the skin surface, a force sensitive resistor (FSR 402) is utilized. The thin-film sensor is sandwiched between the sleeve and the silicone calf mimic. Adjustments are done to guarantee that the pressure change from the DEA is measured accurately. To calibrate the pressure sensor using the data sheet calibration curves, a 10 k Ω resistor is chosen. Using Matlab curve fitting software, data points collected from the sensor's force-voltage curve from the data-sheet are used to estimate a mapping between the voltage and corresponding force, F,

$$F = \left(\frac{V_{out} - c_s}{a_s}\right)^{\frac{1}{b_s}} \tag{48}$$

where V_{out} is the pressure sensor voltage, a_s , b_s , and c_s are the constants to match the factory calibration curve [40]. The values of the constants are 30.77, 0.02073, and -32.1 respectively. The relationship between sensor resistance, input resistor, and output voltage, as provided by the manufacturer data-sheet is

$$V_{out} = \frac{R_M V_{sup}}{R_M + R_{FSR}} \tag{49}$$

where R_M is the selected 10 k Ω resistor, V_{sup} is the 5 V power supply, and R_{FSR} is the variable force sensor resistance. The control voltage is supplied by DSpace to a high voltage amplifier. The amplified voltage is then applied onto the DEA. The voltage applied to the DEA and force change measurement is captured using dSPACE (DS1104) R&D Controller Board. Simulink is used to provide the actuation voltage and to capture output signals.

Given the force, F, the local pressure, P_s can be calculated from the pressure sensor as

$$P_s = \frac{F}{\pi r_z^2} \tag{50}$$

where $r_s = 6.25$ is the radius of the active area of the pressure sensor.

A sinusoidal input signal is used to supply voltage to the DEA. The peak voltage in the input signal is ranged from 10 kV to 17.5 kV for six distinct trials with an input frequency of 0.5 Hz in the first experiment to detect the capillary increase in the plastic tubing as shown in Figure 7.

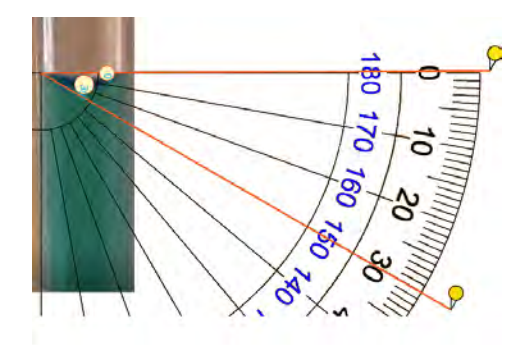


Fig. 7. Capillary contact angle

The pressure from the contact angle change is calculated using the equation

$$P_{\theta_c} = \frac{2\sigma\cos\theta_c}{r} \tag{51}$$

where P_{θ_c} is the capillary pressure, σ is the surface tension of the fluid measured as 0.067 N/m, θ_c is the measured contact angle, and r is the radius of the capillary tube which is 0.0028 m. The change in pressure, ΔP_f can be calculate by taking the difference in the unactuated pressure, P_0 and actuated pressure, P_{θ_c} as follow:

$$\Delta P_f = P_0 - P_{\theta_c} \tag{52}$$

The unactuated pressure is considered to be the pressure at zero contact angle. A relationship between the input voltage and the pressure is observed and shown in Figure 8. Against this is plotted the predicted pressure from the model output y_2 .

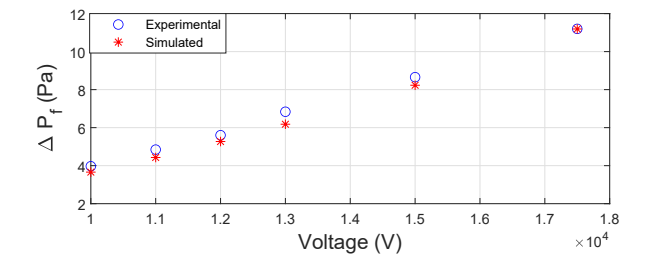


Fig. 8. A comparison of the experimental data and simulation for fluid pressure

B. Model Identification and Validation

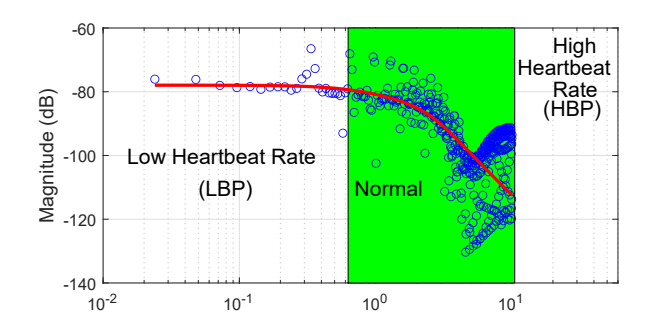
To capture the frequency dependency, a frequency response analysis is carried out on the DECMD as shown in Figure 9. The frequency response function (FRF) is generated using square signals of peak to peak voltage 10, 15, and 18 kV to get the average FRF. Using curve fitting techniques, a third-order transfer function for the DECMD is estimated as

$$G(s)_{DECMD} = \frac{-2.255 \times 10^{-4} s + 7.698 \times 10^{-4}}{s^3 - 2.452s^2 + 3.29s + 6.071}$$
(53)

The choice stems from the assumption that as an electromechanical system, it is first order in it's electrical component and second order in the mechanical component. The system's non-linearity arises from the system output. Model simulation parameters are listed in Table I.

Figure 10 shows the experimental data and simulation for a sinusoidal input of 0.01 Hz, which is measured as force in gf as well as the predicted change in fluid pressure, ΔP_f . The simulation shows adequate approximation to the experimental results in the working frequency range of a normal human pulse. The break down in the estimated model occurs at higher frequencies. In addition, sensor capability limits the precise measurement for small and fast changes in stimuli.

The observed drift at the crests of the force response may be attributed to the viscous effects of the DE as it restores itself when the applied voltage is reduced. Since the dynamics



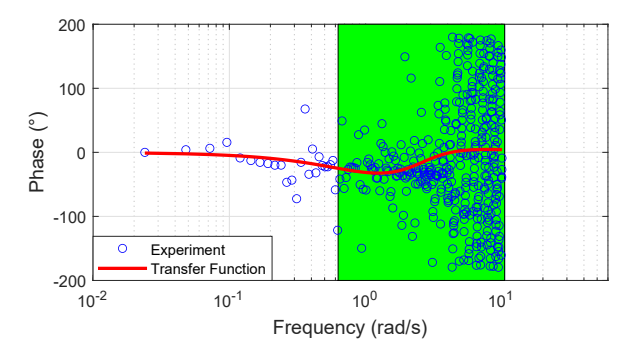


Fig. 9. FRF of the actuator with a transfer function (TF) estimate of one zero and three poles

TABLE I

PARAMETERS USED FOR SIMULATION AND VALIDATION

Parameter	Value	Unit
Н	1	(mm)
Rd	1.91	(cm)
n	2	
μ	30	(KPa)
ϵ_e	4.162×10^{-11}	(F/m)
R	1.0828×10^9	(Ω)
J_m	4.5	
R_m	3.75	(cm)
С	1	(nF)

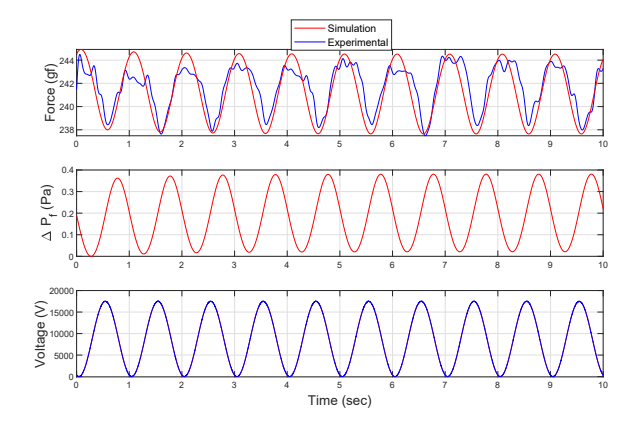


Fig. 10. A comparison of the experimental data and simulation for 1 Hz

of the DE are not fully accounted for in this model, a time delay is also observed between the model response and the experimental results. To account for these effects during control, the ILC is proposed as discussed in section II-C.

C. ILC and PI Experimental Results

To validate the controller for application, and choose a suitable value of γ for the human pulse signal tracking, a sine wave reference signal of amplitude 7.4 gf and frequency of 0.1 and 0.2 Hz are used. PI control is performed to compare with ILC. The performance of the controllers for 0.1 Hz is shown in Figure 11 with $\gamma = 40$. The frequencies are chosen to be close to the pulse pressure variation frequency of the human pulse signal used in the manuscript which is about 0.2 Hz. The pulse pressure variation can be used as a feature to assess and improve blood flow [41], [42].

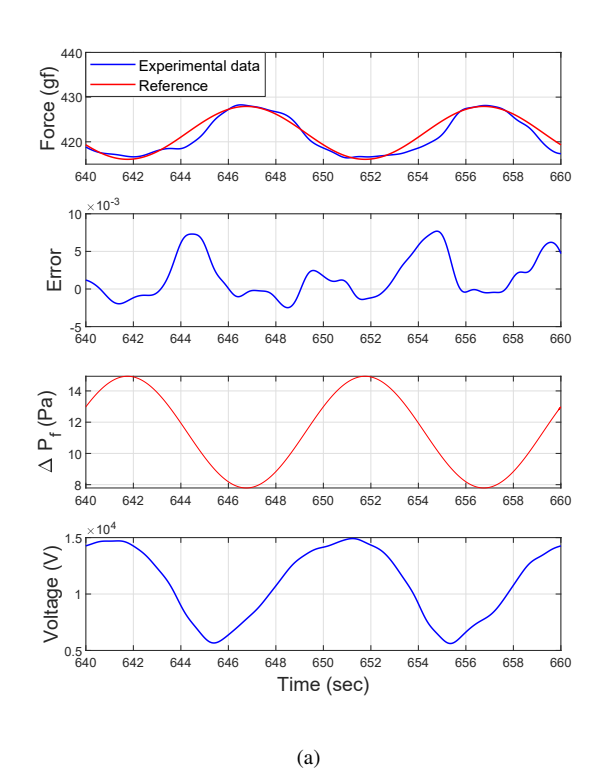
A flushing mechanism is also adopted for the reference signal to generate a square wave based on the human pulse signal. The wave is synchronized by tuning the DEA activation to follow the pressure at a prescribed frequency of systolic peak counts with the pulse pressure variation of the human pulse signal. This variation is closely linked to respiration [43]. The results of such a mechanism are shown in Figure 12. The controller is able to track the reference to within 1.5% error.

IV. CONCLUSION AND FUTURE WORK

A physics model of a DE enabled calf muscle device is described as a control oriented model in this study. The model is validated in the time domain to demonstrate that dynamic actuation is feasible. The model can predict the DECMD's primary characteristic behavior and response. To account for the unmodeled DECMD dynamics, a model based adaptive ILC is designed and implemented to track sinusoidal and human pulse signals. Experimental results have shown that the device can generate up to 10 Pa fluid pressure difference while tracking a human pulse signal with almost zero phase delay and less than 0.02 gf tracking error.

The model dynamics are taken as linear using the RC series circuit and the pressure output is static and nonlinear. The model's accuracy can be increased by accounting for the nonlinear viscous effects. Furthermore, the model's current constraint is that the circumferential stretch is considered to be independent of the applied voltage (it is only radial dependent). This assumption can be loosened to allow for the longitudinal coupling of the electrical and elastic interactions in the DECMD. In addition, the inhomogeneous deformation of the actuator is ignored under the assumption of homogeneous deformation. If inhomogeneous compression is accounted for, the controller would then have multiple time constants. Therefore the accuracy of the controller is affected through the averaging of the various time constants.

Future studies will focus on a full nonlinear dynamic model which considers nonlinear viscous effect and the coupling between electrical and elastic components. In addition, conducting human tests to demonstrate the hypothesis that DECMD can assist calf muscle to enhance blood flow in lower limbs.



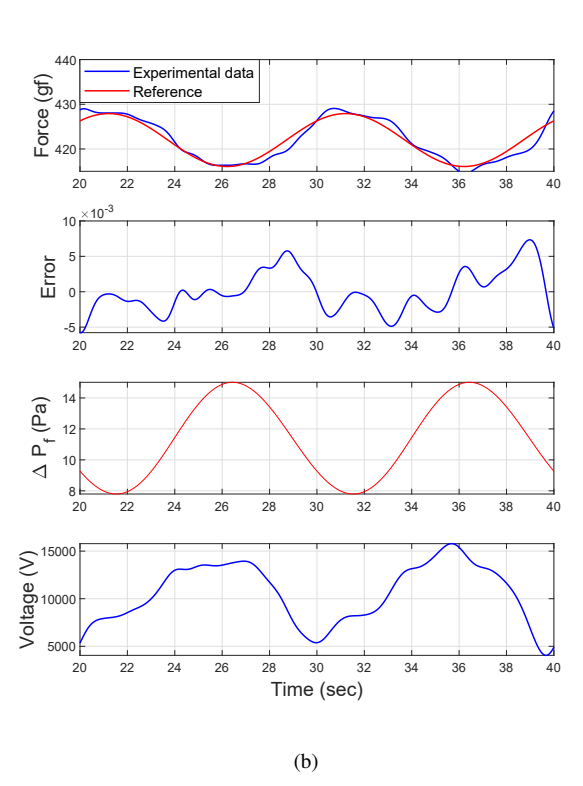


Fig. 11. $\,$ 0.1 Hz sine wave reference signal tracking: a) ILC and b) PI

REFERENCES

- R. E. Mehler, How the circulatory system works. John Wiley & Sons, 2014.
- [2] R. Gupta and P. K. Maurya, "Chapter 1 overview of changes in the cardiovascular system," in *Cardiovascular toxicity and* therapeutic modalities targeting cardio-oncology, I. Qamar and P. K. Maurya, Eds. Academic Press, 2022, pp. 1–10. [Online]. Available: https://www.sciencedirect.com/science/article/pii/B9780323904612000109

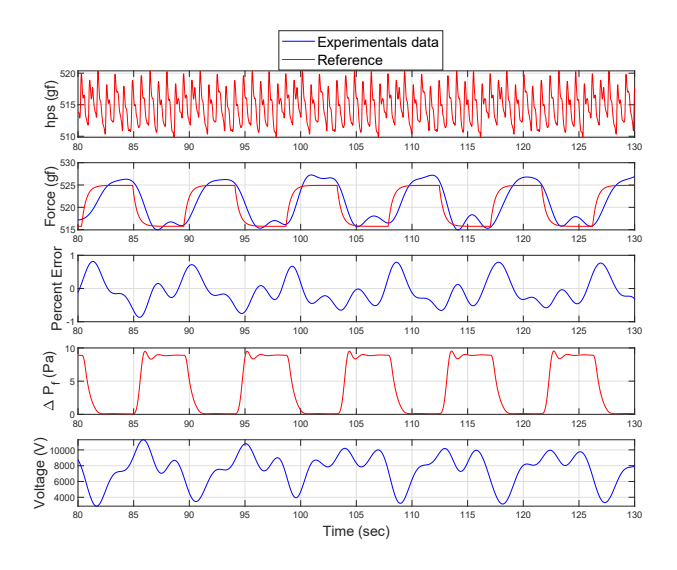


Fig. 12. Flushing Mechanism for DECMD activation tuned to hps

- [3] M. S. Olufsen, J. T. Ottesen, H. T. Tran, L. M. Ellwein, L. A. Lipsitz, and V. Novak, "Blood pressure and blood flow variation during postural change from sitting to standing: model development and validation," *Journal of applied physiology*, vol. 99, no. 4, pp. 1523–1537, 2005.
- [4] P. Jirak, M. Mirna, R. Rezar, L. J. Motloch, M. Lichtenauer, J. Jordan, S. Binneboessel, J. Tank, U. Limper, and C. Jung, "How spaceflight challenges human cardiovascular health," *European Journal* of *Preventive Cardiology*, vol. 29, no. 10, pp. 1399–1411, Feb. 2022. [Online]. Available: https://doi.org/10.1093/eurjpc/zwac029
- [5] J. L. Cameron and A. M. Cameron, Current surgical therapy E-book. Elsevier Health Sciences, 2013.
- [6] R. Klabunde, Cardiovascular physiology concepts. Lippincott Williams & Wilkins, 2011.
- [7] N. Petersen, G. Lambrecht, J. Scott, N. Hirsch, M. Stokes, and J. Mester, "Postflight reconditioning for european astronauts a case report of recovery after six months in space," Musculoskeletal Science and Practice, vol. 27, pp. S23–S31, 2017, terrestrial neuro-musculoskeletal rehabilitation and astronaut reconditioning: reciprocal knowledge transfer. [Online]. Available: https://www.sciencedirect.com/science/article/pii/S246878121630008X
- [8] A.-M. Liphardt, R. Fernandez-Gonzalo, K. Albracht, J. Rittweger, and L. Vico, "Musculoskeletal research in human space flight unmet needs for the success of crewed deep space exploration," npj Microgravity, vol. 9, no. 1, p. 9, Jan 2023. [Online]. Available: https://doi.org/10.1038/s41526-023-00258-3
- [9] S. N. Draper, E. L. Kullman, K. E. Sparks, K. D. Little, and J. Thoman, "Effects of intermittent pneumatic compression on delayed onset muscle soreness (doms) in long distance runners." *International journal of exercise science*, vol. 13 2, pp. 75–86, 2020.
- [10] G. Murthy, D. Watenpaugh, R. Ballard, and A. Hargens, "Exercise against lower body negative pressure as a countermeasure for cardiovascular and musculoskeletal deconditioning," *Acta Astronautica*, vol. 33, pp. 89–96, 1994. [Online]. Available: https://www.sciencedirect.com/science/article/pii/0094576594901120
- [11] K. T. Khieu, L. G. Petersen, and I. R. Hargens, Lower Body Negative Pressure for Artificial Gravity in Space. Cham: Springer International Publishing, 2021, pp. 469–478. [Online]. Available: https://doi.org/10.1007/978-3-319-12191-8_138
- [12] N. Ashari and A. R. Hargens, "The mobile lower body negative pressure gravity suit for long-duration spaceflight," Frontiers in Physiology, vol. 11, 2020. [Online]. Available: https://www.frontiersin.org/articles/10.3389/fphys.2020.00977
- [13] R. J. Venkatraman, T. Kaaya, H. Tchipoque, K. Cluff, R. Asmatulu, R. Amick, and Z. Chen, "Design, fabrication, and characterization of dielectric elastomer actuator enabled cuff compression device," in *Elec*troactive Polymer Actuators and Devices (EAPAD) XXIV, vol. 12042. SPIE, 2022, pp. 32–40.
- [14] Q. Pei, M. A. Rosenthal, R. Pelrine, S. Stanford, and R. D. Kornbluh, "Multifunctional electroelastomer roll actuators and their application

- for biomimetic walking robots," in *Smart Structures and Materials* 2003: *Electroactive Polymer Actuators and Devices (EAPAD)*, vol. 5051. International Society for Optics and Photonics, 2003, pp. 281–290.
- [15] S. Wang and Z. Chen, "Modeling of jellyfish-inspired robot enabled by dielectric elastomer," *International Journal of Intelligent Robotics and Applications*, vol. 5, no. 3, pp. 287–299, 2021.
- [16] ——, "Modeling of two-dimensionally maneuverable jellyfish-inspired robot enabled by multiple soft actuators," *IEEE/ASME Transactions on Mechatronics*, vol. 27, no. 4, pp. 1998–2006, 2022.
- [17] M. Duduta, E. Hajiesmaili, H. Zhao, R. J. Wood, and D. R. Clarke, "Realizing the potential of dielectric elastomer artificial muscles," *Proceedings of the National Academy of Sciences*, vol. 116, no. 7, pp. 2476–2481, 2019.
- [18] G. Kovacs, L. Düring, S. Michel, and G. Terrasi, "Stacked dielectric elastomer actuator for tensile force transmission," *Sensors and actuators* A: *Physical*, vol. 155, no. 2, pp. 299–307, 2009.
- [19] S. Pourazadi, S. Ahmadi, and C. Menon, "Towards the development of active compression bandages using dielectric elastomer actuators," *Smart Materials and Structures*, vol. 23, no. 6, p. 065007, 2014.
- [20] H. Edher, L. Maupas, S. Nijjer, and A. Salehian, "Utilizing tension reduction in a dielectric elastomer actuator to produce compression for physiological application," *Journal of Intelligent Material Systems and Structures*, vol. 29, no. 5, pp. 998–1011, 2018.
- [21] S. Pourazadi, M. Moallem, and C. Menon, "Nonlinear control and simulation of a dielectric elastomer actuator-based compression bandage on flexible human calf," in *Bioinformatics and Biomedical Engineering*, I. Rojas and F. Ortuño, Eds. Cham: Springer International Publishing, 2017, pp. 289–300.
- [22] D. Owens, Iterative Learning Control: An Optimization Paradigm, ser. Advances in Industrial Control. Springer London, 2015. [Online]. Available: https://books.google.com/books?id=krvYCgAAQBAJ
- [23] E. Rogers and O. R. Tutty, "Iterative learning control with applications in energy generation, lasers and health care," *Proceedings* of the Royal Society A: Mathematical, Physical and Engineering Sciences, vol. 472, no. 2193, p. 20150569, 2016. [Online]. Available: https://royalsocietypublishing.org/doi/abs/10.1098/rspa.2015.0569
- [24] S. Mishra and M. Tomizuka, "Projection-based iterative learning control for wafer scanner systems," *IEEE/ASME Transactions on Mechatronics*, vol. 14, no. 3, pp. 388–393, 2009.
- [25] Y. Chen, K. L. Moore, J. Yu, and T. Zhang, "Iterative learning control and repetitive control in hard disk drive industry—a tutorial," *International Journal of Adaptive Control and Signal Processing*, vol. 22, no. 4, pp. 325–343, 2008. [Online]. Available: https://onlinelibrary.wiley.com/doi/abs/10.1002/acs.1003
- [26] S.-C. Wu and M. Tomizuka, "An iterative learning control design for self-servowriting in hard disk drives," *Mechatronics*, vol. 20, no. 1, pp. 53–58, 2010, special Issue on "Servo Control for Data Storage and Precision Systems", from 17th IFAC World Congress 2008. [Online]. Available: https://www.sciencedirect.com/science/article/pii/S0957415809001159
- [27] T. Kaaya, S. Wang, M. Cescon, and Z. Chen, "Physics-lumped parameter based control oriented model of dielectric tubular actuator," *International Journal of Intelligent Robotics and Applications*, vol. 6, no. 3, pp. 397–413, 2022.
- [28] L. Calabrese, G. Frediani, M. Gei, D. De Rossi, and F. Carpi, "Active compression bandage made of electroactive elastomers," *IEEE/ASME Transactions on Mechatronics*, vol. 23, no. 5, pp. 2328–2337, 2018.
- [29] H. Zhao, A. M. Hussain, M. Duduta, D. M. Vogt, R. J. Wood, and D. R. Clarke, "Compact dielectric elastomer linear actuators," *Advanced Functional Materials*, vol. 28, no. 42, p. 1804328, 2018.
- [30] S. Gelman, D. Warner, and M. Warner, "Venous Function and Central Venous Pressure: A Physiologic Story," *Anesthesiology*, vol. 108, no. 4, pp. 735–748, 04 2008. [Online]. Available: https://doi.org/10.1097/ALN.0b013e3181672607
- [31] J. R. Basford, T. R. Jenkyn, K.-N. An, R. L. Ehman, G. Heers, and K. R. Kaufman, "Evaluation of healthy and diseased muscle with magnetic resonance elastography," *Archives of Physical Medicine and Rehabilitation*, vol. 83, no. 11, pp. 1530–1536, 2002. [Online]. Available: https://www.sciencedirect.com/science/article/pii/S0003999302002460
- [32] K. Chino, R. Akagi, M. Dohi, S. Fukashiro, and H. Takahashi, "Reliability and validity of quantifying absolute muscle hardness using ultrasound elastography," *PLoS ONE*, vol. 7, no. 9, 2012.
- [33] J. Sang, S. Xing, H. Liu, X. Li, J. Wang, and Y. Lv, "Large deformation analysis and stability analysis of a cylindrical rubber tube under internal pressure," *Journal of Theoretical and Applied Mechanics*, vol. 55, no. 1, 2016. [Online]. Available: http://ptmts.org.pl/jtam/index.php/jtam/article/view/3232.

- [34] C. T. Herakovich, *Thin-Walled Pressure Vessels*. Cham: Springer International Publishing, 2017, pp. 77–81. [Online]. Available: https://doi.org/10.1007/978-3-319-45602-713
- [35] S. Wang, T. Kaaya, and Z. Chen, "Self-sensing of dielectric elastomer tubular actuator with feedback control validation," *Smart Materials and Structures*, vol. 29, no. 7, p. 075037, jun 2020. [Online]. Available: https://doi.org/10.1088/1361-665x/ab914b
- [36] Z. Ye and Z. Chen, "Self-sensing of dielectric elastomer actuator enhanced by artificial neural network," *Smart Materials and Structures*, vol. 26, no. 9, p. 095056, aug 2017. [Online]. Available: https://doi.org/10.1088/1361-665x/aa7e66
- [37] K. Jung, K. J. Kim, and H. R. Choi, "Self-sensing of dielectric elastomer actuator," in *Electroactive Polymer Actuators and Devices* (EAPAD) 2008, Y. Bar-Cohen, Ed., vol. 6927, International Society for Optics and Photonics. SPIE, 2008, pp. 555 – 564. [Online]. Available: https://doi.org/10.1117/12.776831
- [38] R. Lee, L. Sun, Z. Wang, and M. Tomizuka, "Adaptive iterative learning control of robot manipulators for friction compensation," *IFAC-PapersOnLine*, vol. 52, no. 15, pp. 175–180, 2019, 8th IFAC Symposium on Mechatronic Systems MECHATRONICS 2019. [Online]. Available: https://www.sciencedirect.com/science/article/pii/S2405896319316593
- [39] D. H. Owens, Iterative learning control: an optimization paradigm. Springer, 2015.
- [40] I. Interlink Electronics, "Fsr 402." [Online]. Available https://www.interlinkelectronics.com/fsr-402
- [41] A. C. DORNHORST, P. HOWARD, and G. L. LEATHART, "Respiratory variations in blood pressure," *Circulation*, vol. 6, no. 4, p. 553–558, 1952
- [42] F. Michard and J.-L. Teboul, "Using heart-lung interactions to assess fluid responsiveness during mechanical ventilation," *Critical Care*, vol. 4, no. 5, p. 282, Sep 2000. [Online]. Available: https://doi.org/10.1186/cc710
- [43] A. Perel, R. Pizov, and S. Cotev, "Respiratory variations in the arterial pressure during mechanical ventilation reflect volume status and fluid responsiveness," *Intensive Care Medicine*, vol. 40, no. 6, pp. 798–807, Jun 2014. [Online]. Available: https://doi.org/10.1007/s00134-014-3285-9